

Nanometer-Scale Height Measurements in Micromachined Picoliter Vials based on Interference Fringe Analysis

L.R. van den Doel¹, L.J. van Vliet¹, K.T. Hjelt², M.J. Vellekoop²,
F. Gromball³, J.G Korvink³, I.T. Young¹

¹ Pattern Recognition Group, Lorentzweg 1, Delft University of Technology,
NL-2628 CJ Delft, The Netherlands

² Electronic Instrumentation Laboratory, Mekelweg 4, Delft University of Technology,
NL-2628 CD Delft, The Netherlands

³Institute for Microsystem Technique, Am Flughafen 17, Albert Ludwigs University,
D-79110 Freiburg, Germany

E-mail: L.R.vandenDoel@ph.tn.tudelft.nl

Abstract

Micromachined picoliter vials in silicon dioxide with a typical depth of $6.0\mu\text{m}$ are filled with a liquid sample. Epi-illuminated microscopic imaging during evaporation of the liquid shows dynamic fringe patterns. These fringe patterns are caused by interference between the direct part and the reflected part of an incident plane wave (reflected from the bottom of the vial). The optical path difference (OPD) between the direct and the reflected wave is proportional to the distance to the reflecting bottom of the vial. Evaporation decreases the OPD at the meniscus level and causes alternating constructive and destructive interference of the incident light resulting in an interferogram. Imaging of the space-varying OPD yields a fringe pattern in which the isophotes correspond to isoheight curves of the meniscus. When the bottom is flat, the interference pattern allows monitoring of the liquid meniscus as a function of time during evaporation. On the other hand, when there are objects on the bottom of the vial, the height of these objects are observed as phase jumps in the fringes proportional to their height. First, this paper presents the underlying optical model. Secondly, an image processing method is described to retrieve the meniscus profile from the interference pattern. This algorithm is based on estimating the wrapped (relative) phase of the fringe pattern in the recorded images. Finally, this algorithm is applied to measure height differences on the bottom in other micromachined vials with a precision of about

five nanometer.

1 Introduction

During the evaporation process of a liquid sample in a cubic shaped picoliter vial etched in silicon dioxide with a depth of $6\mu\text{m}$ and a typical size of $300 \times 300\mu\text{m}^2$, the meniscus is pinned in place to the edge of the vial [1]. As a result of the pinning, the air-liquid interface initially, *i.e.* after filling of the vial with the liquid sample, has a convex shape and changes then via flat to a concave shape during evaporation. The thin liquid film with a varying meniscus profile generates a dynamic interference pattern when observed under an epi-illumination microscope, (*even*) with an incoherent narrow-banded unpolarized light source. The isophotes of the fringes in this interference pattern are points of equal liquid height [2]. In Figure 1 a typical interference pattern is shown. This paper presents a method to retrieve the height profile of the liquid during evaporation by analysis of a recorded time series of the interference pattern. The results shows a height profile as a function of time. For proper understanding of the optical phenomenon, a model describing the generation of the interference pattern in the liquid will be introduced.

2 Optical Model

The optical model is shown in Figure 2. After refraction at the air-liquid interface, a plane wave from an incoherent light source, propagates towards a reflecting surface.

A. Sanfeliu, J.J. Villanueva, M. Vanrell, R. Alquézar, T. Huang, J. Serra (eds.), Proc. 15th Int. Conference on Pattern Recognition (Barcelona, Spain, Sep.3–7), vol. 3, Image, Speech, and Signal Processing, IEEE Computer Society Press, Los Alamitos, 2000, 57–62.

1051-4651/00 \$10.00 ©2000 IEEE

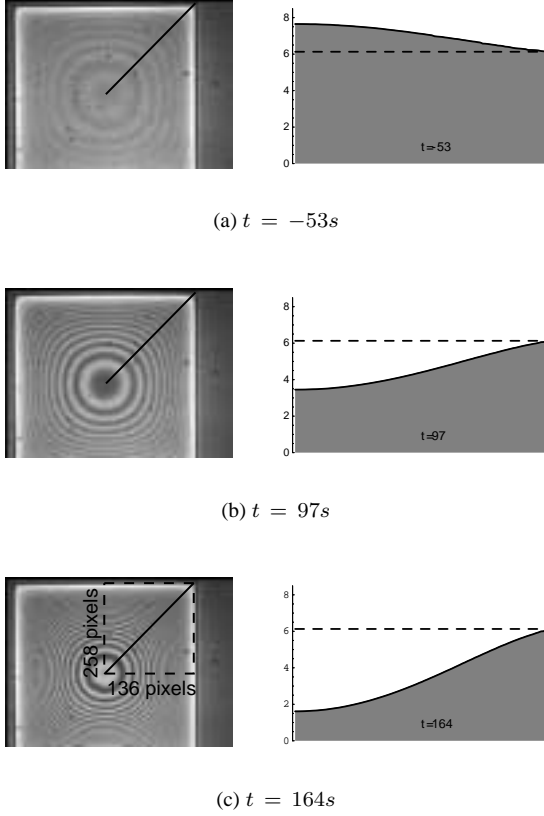


Figure 1. The left figures show the dynamic interference patterns as recorded in a $6.0\mu\text{m}$ deep vial of a microarray. The right graphs show the one-dimensional height profiles (computed as explained in Section 3) along the diagonal as indicated in the bottom left figure. Because of symmetry, the region of interest (136×258 pixels) is only a quarter of the vial.

The main concept of the generation of the interference pattern is the fact that the direct part of an incident plane wave interferes with the part of the incident plane wave that is reflected at the bottom of the vial. The sum of all these single-quantum modulations gives rise to the observed interference pattern [3]. The air-liquid interface is considered to be parallel to the silicon bottom of the vial, as shown in Figure 2.

The optical path difference OPD between the direct part and the reflected part of the incident plane wave at a height d above the reflecting bottom of the vial is given by

$$OPD = 2 n_{liq} d \cos(\Theta_{in}), \quad (1)$$

where n_{liq} is the refractive index of the liquid (ethylene-

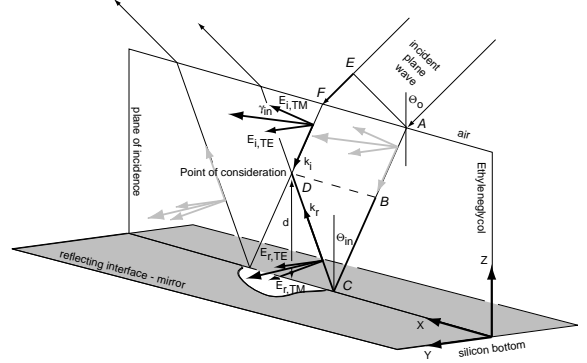


Figure 2. The direct part of the incident plane wave interferes with the part that is reflected from the bottom of the vial. This results in a modulation of the electric field \vec{E} as a function of the height d .

glycol, $n_{liq} = 1.432$), and Θ_{in} is the angle of incidence in the liquid. The phase difference Φ_{in} corresponding to this optical path difference is

$$\Phi_{in} = \frac{4\pi n_{liq} d \cos(\Theta_{in})}{\lambda_{in}}, \quad (2)$$

where λ_{in} is the wavelength of the incident wave.

As indicated in Figure 2, the electric field of the incident wave in the liquid film is split into its TE-components (\vec{E}_{TE} , the electric field perpendicular to the plane of incidence), and its TM-components (\vec{E}_{TM} , the electric field parallel to the plane of incidence). Using the notation from Figure 2, the electric field \vec{E} at the point of consideration is given in Cartesian coordinates by

$$\begin{aligned} \vec{E} &= \vec{E}_i + \vec{E}_r = (\vec{E}_i + \vec{E}_r)_{TE} + (\vec{E}_i + \vec{E}_r)_{TM}, \\ \vec{E} &= E_i \begin{bmatrix} \cos(\gamma_{in}) \cos(\Theta_{in})(1 + r_{TM}e^{i\Phi_{in}}) \\ \sin(\gamma_{in})(1 + r_{TE}e^{i\Phi_{in}}) \\ \cos(\gamma_{in}) \sin(\Theta_{in})(1 + r_{TM}e^{i\Phi_{in}}) \end{bmatrix}, \quad (3) \end{aligned}$$

where γ_{in} is the angle of polarization with respect to the plane of incidence, r_{TE} and r_{TM} are the Fresnel coefficients for reflection for both components of the electric field.

The modulations of the electric field as expressed in Formula 3 are measured with image sensors as modulations in the intensity of the electric field $|\vec{E}|^2$. The first step to compute the intensity of the local electric field in the point of consideration is to integrate $|\vec{E}|^2$ analytically over all angles of polarization. The result can be split into an offset, which will not be further considered, and a modulating part:

$$\langle |\vec{E}|^2 \rangle_{\gamma_{in}} = E_i^2 \pi (2 + r_{TE}^2 + r_{TM}^2 + 2(r_{TE} + r_{TM}) \cos(\Phi_{in})). \quad (4)$$

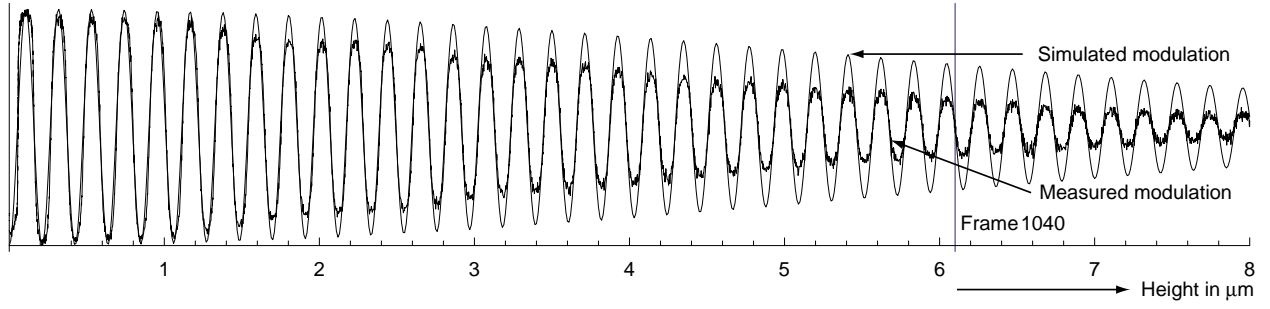


Figure 3. This graph shows the modulation of the strength of the local electric field as a function of the height d above the reflecting bottom of the vial. One curve is based on evaluation of Equation 6, whereas the other curve is experimentally acquired. Frame 1040 corresponds to the time in the recording of the interference pattern where the meniscus is flat.

Formula 4 is the intensity of the electric field summed over all angles of polarization for a single wavelength λ_{in} and a single angle of incidence Θ_{in} .

First, for the experiments, a narrow bandpass filter with a central wavelength $\lambda_c = 602.3nm$ and a FWHM of $9.7nm$ is placed in the illumination path. The transmission spectrum $S(\lambda)$ (normalized in amplitude) of this filter can be approximated by a flattened Gaussian function:

$$S(\lambda) = \left(1 + \frac{(\lambda - \lambda_c)^2}{2\sigma_\lambda^2}\right) \exp\left(-\frac{(\lambda - \lambda_c)^2}{2\sigma_\lambda^2}\right), \quad (5)$$

with $\sigma_\lambda = 2.56nm$ corresponding to the FWHM of the filter.

Second, the angle of incidence Θ_0 is determined by the size of the light source in the congruent back focal plane of the objective lens ($NA = 0.75$). The light source fills one-fifth of this plane. The marginal rays of the incident light contribute most to the interference pattern with a weight function $\tan(\Theta_0)$. The angles of incidence Θ_0 and Θ_{in} are related by Snellius' law.

With these two weight functions, the intensity of the local electric field can be computed as:

$$|\vec{E}(d)|^2 = \int_{\Theta_{in}=0}^{\Theta_{max}} \int_{\lambda=0}^{\infty} \tan(\Theta_{in}) S(\lambda) \langle |\vec{E}|^2 \rangle_{\gamma_{in}} d\Theta_{in} d\lambda, \quad (6)$$

where $S(\lambda)$ as defined in Formula 5 and $\langle |\vec{E}|^2 \rangle_{\gamma_{in}}$ as in Formula 4. The maximum angle of incidence Θ_{max} corresponds to an angle of incidence defined by one-fifth of the NA of the lens.

2.1 Validation of the optical model

Equation 6 is evaluated numerically as a function of the height d above the bottom of the vial with $\lambda_c = 602.3nm$,

$\sigma_\lambda = 2.56nm$, $n_{liq} = 1.4319$, $n_{sil} = 3.95$ and $\Theta_{max} = 0.155rad$. The result of this computation is shown in Figure 3. This computation is compared to measurements in a digital recording (15 frames per second) of an evaporating ethylene-glycol sample. In each frame the intensity in the center of the vial is measured. As can be seen in Figure 1, the meniscus in the center of the vial is always flat because of symmetry, as assumed in the optical model. The modulating intensity, measured as a function of time, is unwrapped with the method to be presented in Section 3. The unwrapping algorithm gives the height of the liquid as a function of time. The combination of the computed height and the measured intensity is also shown in Figure 3. As can be seen in Figure 3 the period of the measured modulation equals the period of the simulated modulation. It is beyond the scope of this paper to show that the length of the modulations Δd equals

$$\Delta d = \frac{\lambda_c}{2n_{liq} \cos(\Theta_{max}^{eff})} \quad (7)$$

where $\Theta_{max}^{eff} = 0.82 \times \Theta_{max}$. The amplitude of the measured modulation, however, drops much faster than that of the simulated modulation. The measurement is much more complicated than the model assumes and is hampered by limited axial resolution in the microscope.

When the air-liquid interface becomes virtually flat the fringes of the interference pattern disappear because the meniscus becomes parallel to the bottom. In this time interval the OPD is approximately independent of the position. Although no fringe pattern is being observed, the measured intensity over the entire vial is influenced by the actual phase difference. This means that the intensity over the entire vial shows the same modulation in time due to the time-varying OPD when the meniscus transites from concave to convex. This has been monitored and is shown in

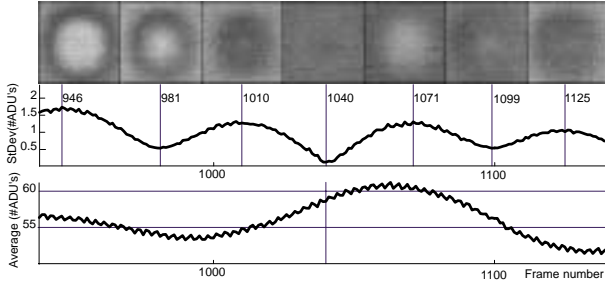


Figure 4. The lowest variation in the average intensity corresponds to the flat meniscus. Within half a period above and below the perfectly flat meniscus, the average intensity should encounter a maximum value.

Figure 4. The bottom graph shows the modulation of the average intensity as a function of time, whereas the top graph shows the variation of the average intensity (measured after background correction). The frame with the smallest variation in average intensity corresponds to the one with the flat meniscus. In this figure, the standard deviation of a frame i is computed as

$$StDev(I_i[m, n] - \langle I[m, n] \rangle_{t=1010\dots1070}), \quad (8)$$

where $\langle I[m, n] \rangle_t$ is the space varying average value over 60 frames in the time span where the meniscus is virtually flat.

3 Unwrapping Algorithm.

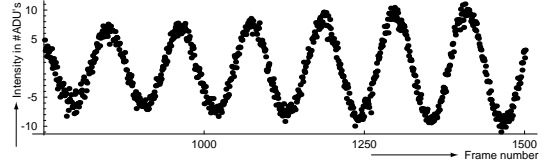
The acquired interference pattern as shown in Figure 1 can be described by [4]:

$$I[m, n; t] = A[m, n; t] \cos(\Phi[m, n; t]) + B[m, n; t] + N[m, n; t], \quad (9)$$

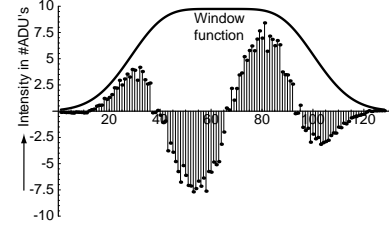
where $A[\cdot]$ and $B[\cdot]$ are the space / time varying amplitude and background. The time-dependency of $A[\cdot]$ is shown in Figure 3. $\Phi[m, n; t]$ is the wrapped phase of the interference pattern as defined in Formula 2 with $d = d(t)$. $N[m, n; t]$ is an additive noise signal.

The absolute or unwrapped phase is related by Formula 7 to the meniscus level. Several algorithms exist that unwrap the phase in 2D images of a fixed interference pattern, e.g. [4, 5]. Since we recorded the interference pattern as a function of time, we propose to unwrap the phase in time point by point.

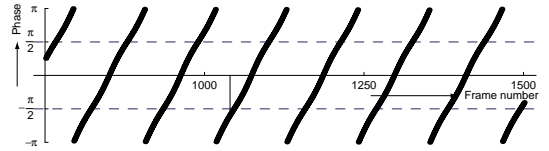
Figure 5 shows the algorithm. The first step in the algorithm is to subtract the background $B[m, n; t]$. The time dependent background is estimated by low pass filtering



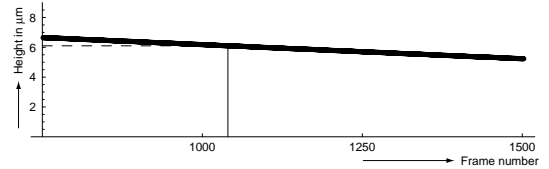
(a) This graph shows the background corrected data $I[t] - A[t]$ in the center point of the vial in the frame series 750 – 1500.



(b) This graph shows the window function $W[t]$ and the product $I_{sub}[t]W[t]$.



(c) This graph shows the estimated phases in the frame series 750 – 1500.



(d) This graph shows the height profile, which follows by unwrapping of the estimated wrapped phases.

Figure 5. The unwrapping algorithm.

$I[t | t = 0 \dots 4572]$ with a Gaussian kernel with a very large standard deviation. Then we compute the number of zero-crossings in $I[t] - B[t]$ to estimate the number of periods of the interference pattern in that point in time. Figure 3 e.g. shows 38 periods in the center point of the vial. However, towards the edge of the vial the number of periods reduces to zero because of the liquid pinning. After filter-

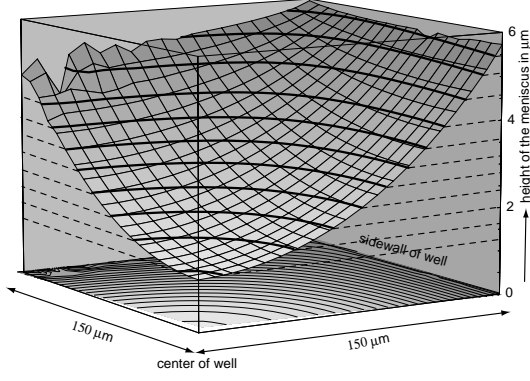


Figure 6. The profile of the meniscus in frame 3750 as computed with the phase unwrapping algorithm in time.

ing $G(t; \sigma) * (I[t] - B[t])$ the number of zero-crossing is counted. The size of the Gaussian filter is increased by a factor of $\sqrt{2}$ until the number of zero-crossings does not change in two successive filterings. From the number of periods follows a factor that is used to subsample the one-dimensional time signal $I[t] - B[t]$. This signal is subsampled to get approximately two periods of the interference pattern in 128 datapoints of $I_{sub}[t]$. This is done to avoid mixing of the low frequency component, the phase of which is to be estimated, with the DC component in the Fourier spectrum. Finally, the phase at a certain moment in time (the central point in the fixed size window of length K_w) is estimated by multiplying $I_{sub}[t]$ with a window function $W[t]$ with a fixed length K_w of 128 points. The window function is defined by

$$W[t] = \left(1 + \frac{1}{2} \left(\frac{t - \frac{K_w}{2}}{\sigma_t}\right)^2 + \frac{1}{8} \left(\frac{t - \frac{K_w}{2}}{\sigma_t}\right)^4\right) \exp\left(-\frac{(t - \frac{K_w}{2})^2}{2\sigma_t^2}\right) \quad (10)$$

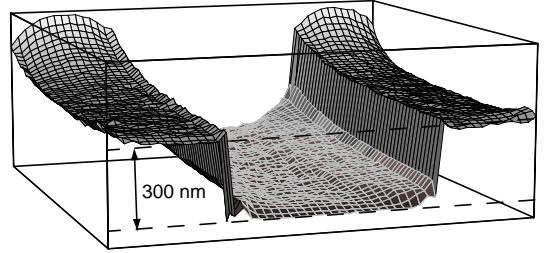
where $\sigma_t = 16.0$. An FFT algorithm is applied to the product $I_{sub}[t]W[t]$. The phase estimate is the phase of the bin with the maximum amplitude in the frequency spectrum.

The result of this algorithm applied to every datapoint in $I_{sub}[t]$ gives the wrapped phase of the interference pattern. Since we have used a one-dimensional algorithm the unwrapping of the wrapped phases is trivial. The unwrapped signal I_{sub}^{unw} is linearly interpolated to its original length. After scaling with $\frac{1}{2\pi}$, Formula 7 converts the absolute phase to a relative height in micrometers. Using two measurements, namely that in frame 1040 the meniscus is flat and that in frame 4572 the liquid reaches the bottom in the center of the vial, the absolute height is defined: the depth of the vial is $6.13\mu m$, as indicated in Figure 3.

The phase unwrapping algorithm in time in a single data point as described above is applied to all data points in the



(a) This image shows the electrodes on the bottom of the vial



(b) This figure shows the retrieved height profile of the electrodes.

Figure 7. The left image shows the frame where the meniscus is flat. The electrodes are clearly visible on the left and right side of the image. The right figure shows the measured height difference between the bottom of the vial and the electrodes on both sides of the vial.

region of interest of 136×258 pixels as indicated in Figure 1. Figure 6 shows the computed height profile of frame 3750.

4 Height Measurements

The unwrapping algorithm in time is applied to measure height differences in other micromachined picoliter vials. In these specific vials two aluminium electrodes have been put on the bottom of the vial. The electrodes introduce a height difference in the vial, which is observed as a phase jump in the interference pattern. The phase jump is computed as follows. First, the interference pattern is recorded and the frame where the meniscus is most likely to be flat is computed as described in Section 2.1. With the method described in Section 3 the *wrapped* phase in each point of this frame is computed. Note that this computation requires 128 frames. The results of this computation makes

the phase jump visible. Again, with Formula 7 the height difference of the electrodes is measured. Since we computed the wrapped phase, the measured absolute height difference limits itself to a maximum of Δd as defined in Formula 7. The result of this computation is shown in Figure 7. We measured the average value and the standard deviation in the computed height profile in three regions $25 \times 25 \text{ pixels}$: the left electrode, the true bottom of the vial and the right electrode. The relative height of the left electrode is $0.289 \mu\text{m}$ with a standard deviation of 4.1 nm . The relative height of the right electrode is $0.282 \mu\text{m}$ with a standard deviation of 4.5 nm . The relative height of the bottom is $0.095 \mu\text{m}$ with a standard deviation of 7.6 nm . The height difference between the bottom and the electrodes is approximately 280 nm . The electrodes have a defined height of $0.3 \mu\text{m}$.

5 Aspects of Sampling

We propose to unwrap the phases in time for each point in the image. There is a fundamental reason to do the unwrapping in time. At the end of the recording (where the meniscus is extremely concave (Figure 1)) the spatial density of the fringes increases, as can be seen in Figure 1. A spatial unwrapping algorithm would encounter sampling problems. Note, however, that because of the pinning of the liquid, the change in height as a function of time is minimal in the region near the edge of the vial. This implies that in this region the phase is more densely sampled in time than in space. Furthermore, spatial unwrapping algorithms will encounter problems in the time span where the meniscus is more or less flat, because no fringes are present there.

The evaporation speed of the liquid, *i.e.* the change in height per unit of time, limits the temporal sampling density. Obviously, the evaporation speed is maximal in the center of the vial. The evaporation speed is defined as the height change of a single fringe Δd in a time span of length $\tau_{\Delta d}$. The analysis requires that approximately two fringes of the temporal fringe pattern correspond to the fixed window width K_w . This requirements yields

$$K_w = 2\tau_{\Delta d}R_{\text{sampling}}, \quad (11)$$

where R_{sampling} is the sampling rate (15 frames per second). Formula 11 can be rewritten as follows:

$$v_{\text{evap.}}^{\text{max}} \leq \frac{2}{K_w} \Delta d R_{\text{sampling}}. \quad (12)$$

On the other hand, the spatial sampling density is limited by the angle α between the meniscus and the bottom of the vial: the projection of the fringes on the image sensor gets denser when the meniscus gets steeper. It can be proven that the phase difference between the two parts of the incident

wave does not depend on the angle between the meniscus and the bottom of the vial. The spatial sampling density SD must satisfy the following equation:

$$\tan(\alpha) \leq \frac{\Delta d}{SD/2}. \quad (13)$$

6 Conclusions and Discussion.

This paper presented a method to retrieve height profiles from recorded time-series of interference patterns. The algorithm unwraps the measured phases in time point by point. As a consequence, all measurements are spatially uncorrelated. A key point in this algorithm is that the recorded interference pattern changes over time and that at some moment a valid reference surface can be chosen. This reference surface is computed where the interference pattern vanishes. The axial resolution is on the order of five nanometer, which is two order of magnitude better than the lateral resolution.

Acknowledgements

This research is supported by the Delft Interfaculty Research Center *Intelligent Molecular Diagnostic Systems*.

References

- [1] R.D. Deegan, O. Bakajin, T.F. Dupont, G. Huber, S.R. Nagel, and T.A Witten. Capillary flow as the cause of ring stains from dried liquid drops. *Nature*, 389:827–829, 1997.
- [2] M. Born and E. Wolf. *Principles of Optics, 6th ed.* Pergamon Press, Oxford, England, 1980.
- [3] A. Lambacher and P. Fromherz. Fluorescence interference-contrast microscopy on oxidized silicon using a monomolecular dye layer. *Applied Physics A, Material Science and Processing*, 63:207–216, 1996.
- [4] M. Servin, F.J. Cuevas, D. Malacara, J.L. Marroquin, and R. Rodriguez-Vera. Phase unwrapping through demodulation by use of the regularized phase-tracking technique. *Journal of Applied Optics*, 38:1934–1941, 1999.
- [5] J. Strand and A.K. Jain. Two-dimensional phase unwrapping using a block least-squares method. *IEEE Transactions on Image Processing*, 8:375–386, 1999.